Composites Science and Technology 72 (2012) 1408–1415

Contents lists available at SciVerse ScienceDirect

Composites Science and Technology

journal homepage: www.elsevier.com/locate/compscitech

Effect of the POSS–Polyimide nanostructure on its mechanical and electrical properties

R. Verker [a,b,*], E. Grossman [a], N. Eliaz [b]

[a] Space Environment Department, Soreq NRC, Yavne 81800, Israel
[b] School of Mechanical Engineering, Tel-Aviv University, Tel-Aviv 69978, Israel

ARTICLE INFO

Article history:
Received 28 November 2011
Received in revised form 5 April 2012
Accepted 9 May 2012
Available online 17 May 2012

Keywords:
A. Nano composites
B. Fracture
B. Impact behavior
B. Electrical properties

ABSTRACT

Nanocomposite films consisted of Polyhedral Oligomeric Silsesquioxane (POSS) filler in a Polyimide (PI) matrix were prepared. The effect of the nanocomposites' structure on its mechanical and electrical properties was evaluated with respect to survival in the low Earth orbit (LEO) environment. The POSS–PI structure consists of POSS nano-aggregates formed in the bulk and on the surface. The aggregates' size and distribution are POSS content-dependant. The fracture mechanism during hypervelocity impact at extreme temperature conditions was studied. The hypervelocity impacts of the POSS–PI films result in a brittle fracture, compared to ductile fracture in the case of PI, and in formation of radial cracks. A model based on formation and coalescence of voids around the aggregates, when load is applied, is suggested to explain the effect of the POSS content on the POSS–PI fracture mechanism. The size and density of the POSS aggregates also affect the nanocomposite's volume electrical resistivity. An inverse dependence exists between the POSS aggregates' surface density and the nanocomposites' volume electrical resistivity.

1. Introduction

Numerous satellites are being launched into the low Earth orbit (LEO) environment, i.e. at altitudes ranging from 200 km to 1000 km. The degrading environment in LEO includes atomic oxygen (AO), ultraviolet (UV) and ionizing radiation, ultrahigh vacuum (UHV), thermal cycling (±100 °C every 90 min.), and hypervelocity micrometeoroids and orbital debris [1–3]. The illumination of satellites by photons results in differential charging of the sunlit surfaces with respect to the shaded portions. This may result in buildup of large potentials on spacecraft and can present a serious electrostatic discharge (ESD) concern since upsets of electronics, detectors degradation and structural damage are real possibilities [4]. The breakup of satellites, either deliberately or accidentally, leads to an increasing amount of orbital debris, which further leads to additional events of hypervelocity impacts onto external satellite surfaces. The development of materials which can sustain such impacts and still function under the harsh conditions of the LEO environment is therefore needed.

Polyimides (PIs) are used extensively in external spacecraft surfaces as thermal blankets and in solar arrays [5,6]. Unprotected PI experience severe erosion when exposed to the LEO environment [7]. SiO_2 coatings have been shown to provide protection for PI against AO attack; however, inherent or hypervelocity debris-induced defects in the coating allows for AO penetration and attack of the underlying polymer [8].

In the past two decades, polymer based nanocomposites have attracted a great deal of interest because they may exhibit substantially improved physical and mechanical properties. These materials represent a novel class of materials that are reinforced by one or more types of fillers, of which at least one dimension of the dispersed particles in the polymer matrix is on the nanometer scale [9].

A promising approach toward the production of LEO survivable polymer-based nanocomposites is incorporation of inorganic Polyhedral Oligomeric Silsesquioxane (POSS) into the polymer matrix [10–12]. POSS molecules are based on a three-dimensional cage-like structure, surrounded by tailorable organic groups. If chosen correctly, these functional groups on the POSS monomers allow them to be copolymerized, grafted, and blended into traditional polymer systems. The POSS nanostructures can be dispersed throughout the polymer matrix, and be synthesized. POSS-containing PIs have shown significantly lower AO erosion yields than pure PI, since AO irradiation results in formation of a SiO_2 passivation layer, which protects the polymer from further AO attack [10].

The fractography of commercial PI (Kapton-HN) film subjected to hypervelocity impacts was studied in detail elsewhere [13]. In other previous studies, PI and POSS–PI nanocomposite films were

* Corresponding author at: Space Environment Department, Soreq NRC, Yavne 81800, Israel.
E-mail address: rverker@soreq.gov.il (R. Verker).

0266-3538/$ - see front matter © 2012 Elsevier Ltd. All rights reserved.
http://dx.doi.org/10.1016/j.compscitech.2012.05.014

exposed to hypervelocity impacts at room temperature (RT) and subsequently to air RF plasma (which simulates an AO environment) [14]. After the hypervelocity impacts, 15 wt.% POSS–PI films revealed higher AO resistance, and its erosion rate was one order of magnitude lower compared to that of PI films. The lower erosion rate was attributed to both mechanical (i.e. no residual tensile stresses) and chemical (i.e. formation of an oxide passivation layer) factors [14].

The different response of PI and POSS–PI to ground simulated hypervelocity impacts performed at RT and subsequent AO exposure motivated a fundamental study of the mechanical properties, surface morphology and chemical composition of these materials [14]. However, this study did not take into account the possible effect of temperature variation, which could range from −100 °C up to +100 °C, due to thermal cycles in LEO. The effect of the POSS–PI nanostructure on its mechanical properties under such extreme temperatures during hypervelocity impacts has not yet been determined.

In previous studies, other types of POSS–PI nanocomposites were shown to have lower dielectric constant compared to the pristine PI [15,16]. However, the electrical properties of the material presented here (see Section 2.2) have not been fully investigated.

The objectives of the present work were to determine the effect of the POSS–PI nanostructure on the fracture mechanism during hypervelocity impacts on POSS–PI thin films maintained at extreme temperatures, as well as on its electrical properties. Such an understanding is essential for development of new types of space hybrid materials for completing successful spacecraft missions. Such a tailored hybrid-material will endure AO attack and hypervelocity impacts through self-passivation ability and improved toughness, combined with enhanced electrical conductivity designed to withstand ESD effects resulting from the extreme LEO space environment.

Characterization of the surface morphology and the fracture surfaces was used to depict the POSS–PI nanostructure. The electrical properties of the POSS–PI nanocomposite, namely its volume electrical resistivity, were investigated via current–voltage characterization using autoranging picoammeter and electrostatic force microscopy (EFM). Based on the given results, the different fracture mechanisms for PI and POSS–PI are established and the effect of the nanostructure on the mechanical and electrical properties is presented.

2. Experimental apparatus and procedure

2.1. The laser-driven flyer method

A laser-driven flyer (LDF) method was used for generating simulated space hypervelocity debris [17–19]. A full description of the principle of operation of this system was given in a previous work [13]. Generally, the LDF system accelerates an aluminum layer, 1 mm in diameter, to a hypervelocity of up to 3 km/s. The LDF system was equipped with a specially designed sample holder that was capable of changing the sample's temperature in a wide range of temperatures, from −60 °C to +100 °C. The sample holder was cooled down by flowing dry nitrogen through a heat-exchanger immersed in a liquid nitrogen bath, or heated up by using a resistive filament attached to a power supply.

2.2. Materials and film preparation

The materials studied in this work were blends of oxydianiline (ODA)-pyromellitic dianhydryde (PMDA) PI (Pyre-M.L. RC-5019 by Industrial Summit Technology, Co.) and trisilanolphenyl (TSP)-POSS (Hybrid Plastics, Inc.). Scheme 1a and b depict the PMDA–ODA PI monomer and TSP-POSS molecule, respectively. There are dozens of commercially available different derivatives of POSS molecules. TSP-POSS was chosen for this work for its compatibility with the ODA–PMDA–PI chain. This compatibility is found through hydrogen bonds formed between the POSS silanol groups and the PI's carbonyl groups. The silanol groups also enable some inter-POSS chemical reaction through silanol–silanol condensation [20].

Samples were produced in the form of thin films, 25–30 μm thick. POSS–PI films with content of 0 (pure PI), 5, 10 and 15 wt.% POSS were produced using a bench-scale process of casting and curing a pre-mixed solution of polyamic acid and POSS in N-methyl-pyrrolidone (NMP) solvent. The curing of the pre-mixed solution is based on a process developed by DuPont, Inc. After casting the pre-mixed solution into a glass mold, the samples were heated to 200 °C in air, at a heating rate of 4 °C/min, and held for a period of 30 min. In a second temperature cycle, the samples were heated to 350 °C in the presence of pure nitrogen, at a heating rate of 2 °C/min, and held for a period of 60 min. In order to minimize residual stresses, the final stage was slow cooling at a rate of 2 °C/min, down to RT [21]. At RT, the PI and POSS–PI films were peeled off the mold.

2.3. Characterization techniques

The morphology of fracture surfaces was studied using an Environmental Scanning Electron Microscopes (ESEM; Models Quanta 200 and 200F (High Resolution SEM (HRSEM)) from FEI). These microscopes allow characterization of degassing and non-conductive samples, such as PI and POSS–PI samples, without the need for conductive coating.

Volume electrical resistivity measurements of the samples were derived from *I–V* measurements. 25 μm-thick samples were cut into discs with 12 mm diameter, which were placed between two metallic electrodes under a constant load. The two electrodes were connected in series to a DC power supply (Model RLPS1–150R from DEL) and a picoammeter (Model 485 from Keithley). Using this configuration, various electrical fields were applied between the electrodes, and current measurements were obtained.

Electrostatic force microscopy (EFM) measurements were performed using the EFM mode of the AFM (MultiMode, Nanoscope IV from Veeco). The samples were scanned using an Antimony doped Si cantilever tip coated with a thin Cr layer. Topographical measurements and electrical data were obtained by the two-pass Lift Mode technique. In this method, during the first pass, the tip operates in Tapping Mode to scan a topographical line and obtain a height image. In the second scan, the cantilever is lifted to a predefined distance of 10–100 nm in order to minimize the effect of the van der Waals forces. During this lift, the cantilever is biased (12 V DC) and detects the variations in the electrical force gradient over the same line while ruling out the influence of surface topography [22].

3. Results

3.1. Hypervelocity impacts

Fig. 1 demonstrates the effect of POSS content and impact velocity on the extent of damage of hypervelocity impacted PI and 15 wt.% POSS–PI. The fractures were created using flyer velocities of either 2.1 km/s (Fig. 1a and c) or 2.9 km/s (Fig. 1b and d). Both samples had the same thickness of 26 μm. The hypervelocity impacts were performed while the sample's temperature was maintained at RT. The 5 wt.% and 10 wt.% POSS–PI impacted samples are not shown since they exhibit the same fractography as the 15 wt.% POSS–PI.

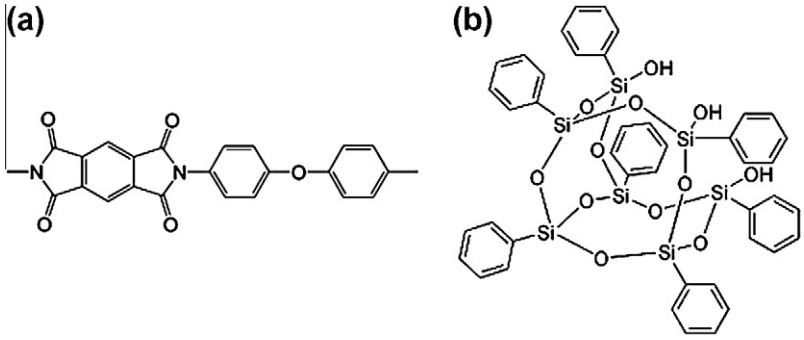

Scheme 1. Schematic presentation of PMDA-ODA PI monomer (a) and TSP-POSS molecule (b).

A comparison of the hypervelocity impacts on the PI film to those on the 15 wt.% POSS–PI film reveals that adding POSS to the PI does not change significantly the extent of damage created by the impact in terms of the perforated area. However, under the same impact conditions, the POSS-containing sample shows a more brittle fracture surface, via formation of radial cracking. The length of the radial cracks increases as the velocity of the impact is raised.

The effects of the samples' temperature as well as the POSS content on the extent of damage of impacted PI and 15 wt.% POSS–PI films is demonstrated in Fig. 2. The fractures of PI and 15 wt.% POSS–PI films (26 μm thick) were created at various sample temperatures of −60 °C (Fig. 2a and b), RT (Fig. 2c and d), and 100 °C (Fig. 2e and f). Fig. 2g and h show ESEM images of the central impact region of the PI and 15 wt.% POSS–PI samples, respectively, that were impacted at 100 °C. The flyer impact velocity was not measured during these experiments; however, according to previous measurements, it was estimated to be around 3 km/s.

In terms of the perforated area, at temperatures of −60 °C, RT and 100 °C, the PI film presents similar results. In general, in all three PI samples the fracture surfaces around the central impact region are ductile in nature. At all three temperatures, the formation of perforation was due to film ripping and bending, and not film shearing. However, the amount of ductility of the PI sample that was maintained at 100 °C (Fig. 2e) is higher compared to the two lower temperatures (Fig. 2a and c).

Analysis of the 15 wt.% POSS–PI film fractography is not as trivial as in the case of PI. At RT the perforated area of the 15 wt.% POSS–PI film resembles the perforated area of the PI sample, in agreement with the results presented in Fig. 1. However, at −60 °C and 100 °C the perforated areas are much larger.

Fig. 2g (PI) and h (15 wt.% POSS–PI) reveal a clear difference between the two samples impacted while maintained at 100 °C. The fracture surface of the PI sample is ductile, characterized mainly by elongated ligaments emanating from the fracture surface. The fracture surface of the 15 wt.% POSS–PI sample can be described as spongy in nature, and the existence of voids is evident. The different fractography and its relation to the POSS–PI nanostructure will be discussed below in Section 4.

3.2. The POSS–PI nanostructure and failure mechanism

The influence of the POSS–PI nanostructure on its failure mechanism is shown in Fig. 3.

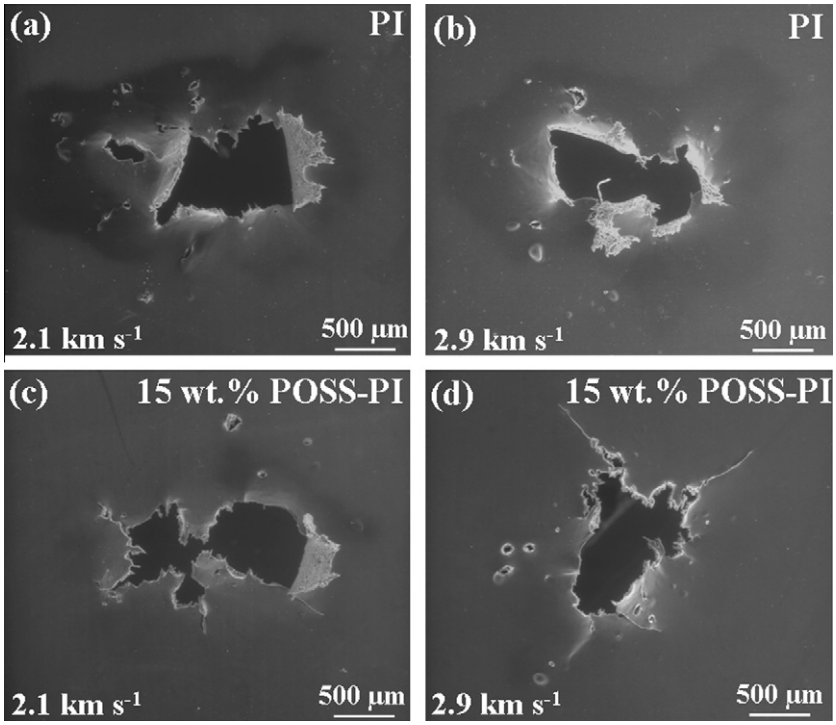

Fig. 1. ESEM images of 26 μm-thick PI (a and b) and 15 wt.% POSS–PI films (c and d), impacted by flyers at velocities of 2.1 km/s (a and c) and 2.9 km/s (b and d).

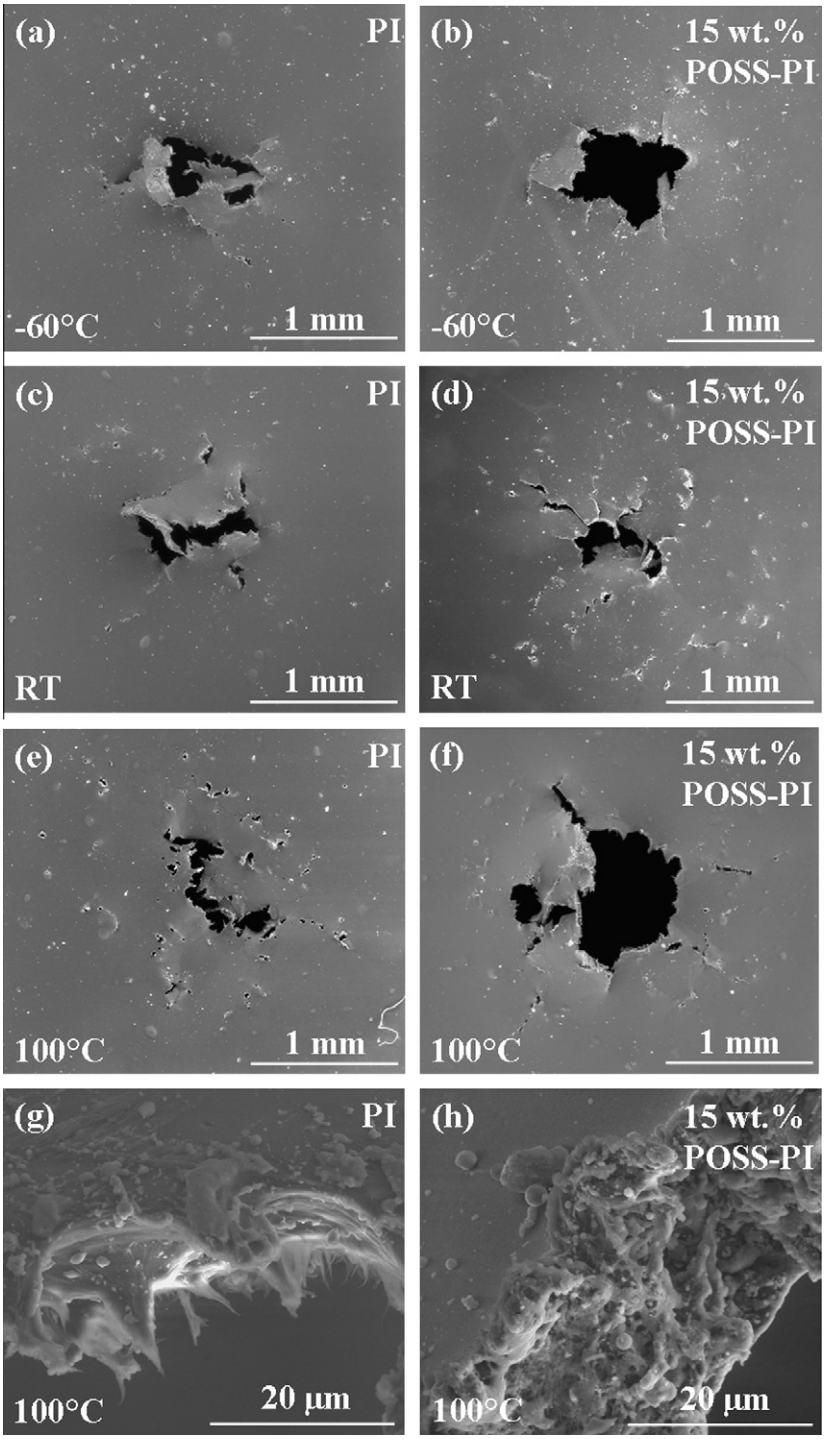

Fig. 2. ESEM images of 26 μm-thick PI (a, c, e, and g) and 15 wt.% POSS–PI (b, d, f, and h) films, maintained at temperatures of −60 °C (a and b), RT (c and d) and 100 °C (e, f, g, and h), impacted by flyers at a velocity of about 3 km/s. Fig. 2g and h are high-magnification ESEM images of Fig. 2e and f, respectively.

Fig. 3 shows HRSEM fractography images of PI (Fig. 3a) and 5 wt.% (Fig. 3b), 10 wt.% (Fig. 3c) and 15 wt.% (Fig. 3d) POSS–PI thin films that were fractured under mode III, out-of-plane shearing. Mode III, out-of-plane shearing occurs when a shear stress is acting parallel to the plane of the crack and parallel to the crack front [23].

The fracture surface of the PI and the 5 wt.% POSS–PI samples is smooth, showing no irregular features. The fracture surfaces of the 10 wt.% and the 15 wt.% POSS–PI films reveal that aggregates are spread inside the bulk of the material. The fracture surfaces of the 10 wt.% and 15 wt.% POSS–PI films are also characterized by the formation of voids around these aggregates.

POSS–POSS interaction via chemical condensation or via physical aggregation was demonstrated previously [20]. This phenomenon was supported by surface morphology obtained using AFM, showing that POSS–PI samples are characterized mainly by the appearance of aggregates on the surface. Increase of the POSS content resulted in an apparent increase in the aggregates' size and surface density. The differences in the aggregates' surface density

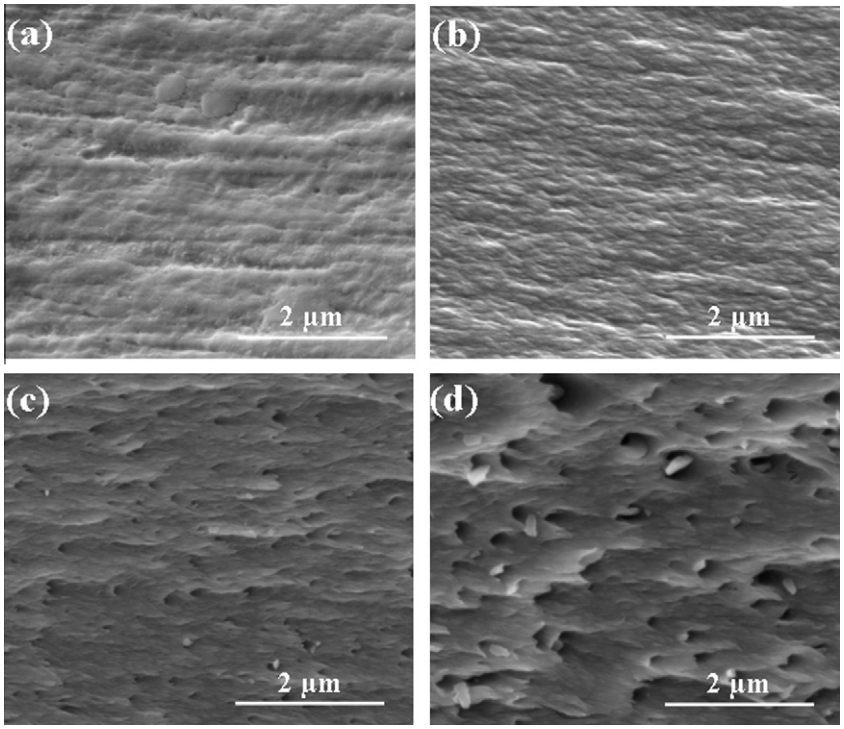

Fig. 3. HRSEM images of the fracture surfaces of PI (a) and 5 wt.% (b), 10 wt.% (c) and 15 wt.% POSS–PI (d) films. The fracture surfaces were obtained using mode III, out-of-plane shearing.

have an effect on the mechanical properties of the nanocomposite [24] as well as on its electrical properties, as will be further discussed in Section 4.

The appearance of aggregates on the surface and inside the bulk of the POSS–PI may be associated with its brittleness, compared to PI, as will be further discussed.

The ability of the POSS aggregates to debond and to be pulled out of the PI matrix is demonstrated most profoundly in Fig. 3d. The formation of voids around the POSS aggregates and the concentration of these voids play an important role in understanding the different mechanical properties of the various POSS–PI compositions and their response to the hypervelocity impacts.

A previous work which studied the failure mechanism of POSS–PI during tensile tests also showed voids formation through debonding of POSS aggregates from the PI matrix upon loading of the sample. Also, it was found that the failure mechanism is associated with coalescence of small voids into large ones during the tensile process [20], as will be further discussed in Section 4.

3.3. POSS–PI electrical properties measurements

Fig. 4 shows the results of volume electrical resistivity measurements of the four types of samples, as obtained from *I–V* measurements. The results depict the effect of POSS addition on the volume electrical resistivity. These results are in agreement with previous measurements executed on silica–PI composites [25,26]. However, unlike these earlier measurements that showed monotonic decrease of volume electrical resistivity with increased silica filler content, the POSS–PI resistivity measurements attain an optimum at 10 wt.% POSS–PI composition.

Fig. 4 also presents the POSS aggregates' surface density ρ_s, obtained by image analysis from AFM surface morphology measurements. These results show an inverse dependence between the volume electrical resistivity of the nanocomposite and the aggregates' surface density. The 10 wt.% POSS–PI attains the highest

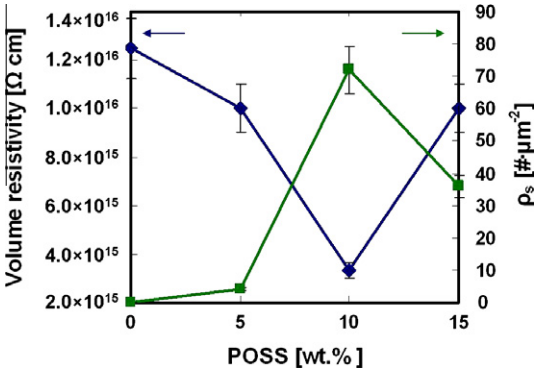

Fig. 4. The volume electrical resistivity and POSS aggregates' density (ρ_s) as a function of POSS content.

average aggregates' surface density of 72 aggregates/μm^2 and the smallest average inter-aggregate distance of 87 nm. The average inter-aggregate distance of the 5 wt.% and 15 wt.% POSS–PI samples was 200 nm and 103 nm, respectively [20]. Correspondingly, the 10 wt.% POSS–PI volume electrical resistivity reaches the lowest level of 3.0×10^{15} Ω cm, compared to that of PI that attains the highest volume electrical resistivity of about 1.3×10^{16} Ω cm. The volume electrical resistivity of the 5 wt.% and 15 wt.% POSS–PI samples shows intermediate values of 1.0×10^{16} Ω cm.

The mechanism that leads to the decrease in volume electrical resistivity of the POSS-containing samples is revealed in Fig. 5, which shows EFM images of 10 wt.% POSS–PI film. Fig. 5a shows a height image obtained in a tapping mode. Fig. 5b and c show phase images of the same area obtained in a lift mode under a tip DC bias voltage of 0 V and 12 V, respectively. Fig. 5a shows two relatively large POSS aggregates having a diameter of about 80 nm each, and an inter-aggregate distance of 70 nm. Under a tip DC bias voltage of 0 V no EFM image is obtained (Fig. 5b).

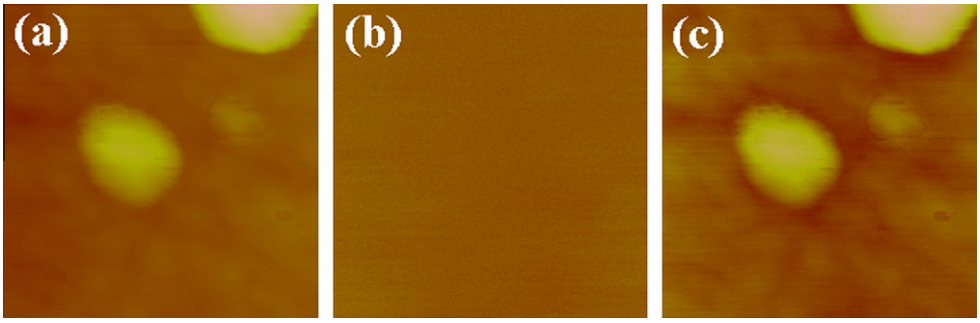

Fig. 5. 10 wt.% POSS–PI film AFM height tapping mode image (a), and EFM phase imaging mode under 0 V (b) and 12 V (c) DC bias. Scan size: 250 × 250 nm. The EFM images were acquired at lift mode at a distance of 100 nm.

However, application of a 12 V bias (Fig. 5c) results in an image which origins from electrical charge distribution. In the EFM image of Fig. 5c, a darker color represents higher charge concentration. It is clearly seen that the electrically active regions are around the boundaries of the aggregates. Electrically active regions can also be noticed to emanate in radial direction from the aggregate placed at the center of the image.

4. Discussion

PI and POSS–PI nanocoposites were prepared in the form of thin films by a bench-scale process which is based on casting and curing of a pre-mixed solution of polyamic acid and POSS in NMP solvent [24]. The effects of POSS content, impact velocity and temperature on the extent of damage of hypervelocity impacted PI and 5 wt.%, 10 wt.%, and 15 wt.% POSS–PI thin films were examined. The impacted samples were analyzed in terms of the perforated area, the type of fracture surface and the formation of cracks.

The effect of the impact velocity at RT on the amount of damage of impacted PI and POSS–PI films is demonstrated in Fig. 1. At RT hypervelocity impacts, both PI and 15 wt.% POSS–PI, the latter representing similar results to those of the 5 wt.% and the 10 wt.% POSS–PI films, are unaffected by the increased impact velocity and reveal similar perforated area. However, under the same impact conditions, the POSS-containing samples show a more brittle fracture surface, via formation of radial cracks, compared to the PI sample.

Under RT hypervelocity impact conditions, PI fails through bending of the film from the central impact region outward. The POSS–PI samples, represented by a 15 wt.% POSS–PI film, show in addition, shearing of film segments and formation of radial cracks. The length of these radial cracks increases at about one order of magnitude as the impact velocity increases from 2.1 km/s to 2.9 km/s. In terms of fractogrphy, the increase in the length of the radial cracks is the only apparent response to the increased impact velocity.

It is suggested that the cause for the formation of radial cracks is that during the hypervelocity impact, tensile stresses are developed parallel to the film plane. The radial cracks, which are evident in Fig. 1c and d, propagate perpendicular to these stresses. The toughness of PI is high enough to resist the formation of radial cracks. In contrast, the toughness of the POSS–PI samples is lower, causing the formation of radial cracks even at the lowest impact velocity [24].

Brittleness of various compositions of POSS–PI compared to PI was found previously in basic tensile tests performed at 450 °C, above the material's *Tg*. Generally, addition of POSS to the PI matrix resulted in lower tensile strength and elongation at break [24]. The cause of this reduction in toughness was evaluated from FTIR spectroscopy [20], AFM measurements and HRSEM surface morphology images. FTIR spectroscopy gave an indication to a network of Si–O–Si groups, which are the result of POSS–POSS reaction via chemical condensation or physical aggregation. Si–O–Si networking forms due to the elevated temperature during the curing process of the POSS–PI [20].

POSS aggregates form on the surface of the POSS–PI film, as shown by the AFM images in Fig. 5. Aggregates are also spread inside the bulk of the material, as can be seen in HRSEM image (Fig. 3).

The formation of voids around the POSS aggregates (Fig. 3c and d) and the coalescence of these voids play an important role in the mechanical response of POSS–PI samples to hypervelocity impacts, as discussed below.

Ojeda and Martin [27] have shown that the morphology of PMDA–ODA PI consists of spherulitic bundles of well-defined lamellae, similar to those typically observed in semi-crystalline polymers [27]. Applying a shear force on the PI film resulted in crack propagation that was initiated mainly between the crystalline lamella structures, where the mobility of the chains is higher, as illustrated in Scheme 2a.

During the hypervelocity impact, shear forces act on the films at the central impact region. In the case of POSS–PI the existence of POSS aggregates beside lamella structures cause a different failure mechanism, compared to PI. Based on existing theories regarding failure mechanisms of particulate-filled polymers [28,29], the effect of the aggregates' diameter, density and inter-aggregate distance on the mechanical properties of the POSS–PI is illustrated in Scheme 2b.

Scheme 2 shows a graphical shear failure model of the PI and POSS–PI different fracture modes. The PI structure (Scheme 2a) consists of crystalline lamellar structures and amorphous (white) regions. When the shear force was applied on the PI film, the polymer fractured, and the crack propagation occurred between lamella sites. Scheme 2b shows the POSS–PI schematic illustration, which includes POSS aggregates besides the lamella structures. While applying the shear force, the POSS aggregates debond from the PI matrix, leading to the formation of voids around the aggregates as the polymer is plastically deformed. The small inter-aggregate distance and the relatively large aggregate diameter lead to lateral coalescence of the voids at early stages. Coalescence into critical-size voids may occur at any location along the gauge section, as shown in Scheme 2b.

This failure process is accompanied by high local stress acting on the thin ligaments between the aggregates. The lateral coalescence of the voids reduces the POSS–PI samples' ability to withstand the loads. When the thin ligaments cannot support the load anymore, they fracture.

The effect of temperature on the fractography of PI and POSS–PI under hypervelocity impacts was examined at temperatures of −60 °C, RT and 100 °C. In the case of PI, the effect of the temperature is evident in terms of radial cracking and ductility (Fig. 2a, c,

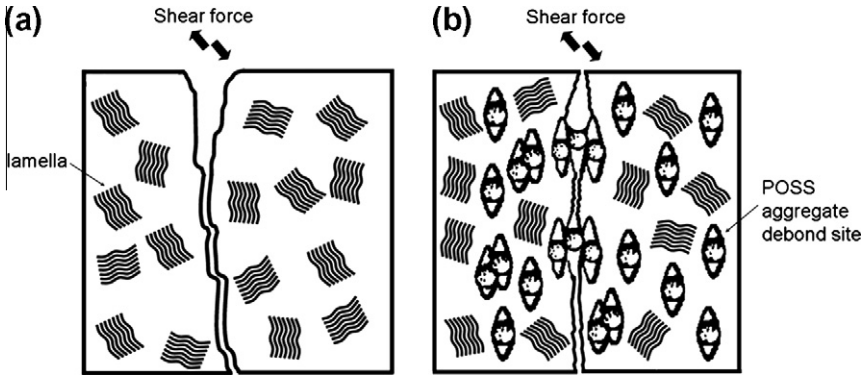

Scheme 2. Schematic presentation of the fracture mechanisms of PI (a) and POSS–PI (b).

and e). In general, for PI samples impacted at any temperature, the fracture surfaces around the central impact region are ductile (based on high-magnification images not shown herein) due to the elevated temperature developed during the impact [13]. However, the amount of ductility of the PI sample impacted at 100 °C (Fig. 2e and g) is higher compared to samples impacted at lower temperatures. The higher ductility can be explained by the high mobility and elongation established in the PI chains due to the additional heat applied to the sample at 100 °C. This given further heating allowed the PI chains a higher degree of freedom in terms of chain stretching. At −60 °C, the effect of temperature is seen by radial cracks that were formed around the central impact point. The cause of this phenomenon is the reduction in PI's fracture toughness and elongation at break as the temperature is decreased [30].

The fractography assessment of the 15 wt.% POSS–PI films, which represent also the 5 wt.% and the 10 wt.% POSS–PI samples, is more complicated compared to that of PI. The perforated areas of the 15 wt.% POSS–PI samples impacted at −60 °C and 100 °C are much larger compared to the RT impact, as shown in Fig. 2b, d, and f. The susceptibility of the 15 wt.% POSS–PI film to hypervelocity impacts at extreme temperatures can be related to its nanostructure. The fracture mechanism of void formation around the POSS aggregates and coalescence of these voids is used to explain the mechanical response of POSS–PI to impacts at extreme temperatures.

At RT, the perforated area of the 15 wt.% POSS–PI film resembles the perforated area of the PI sample, in agreement with the results presented in Fig. 1. Under RT impact, the formation of the perforated area is due to film rippling and bending. Under extreme temperature impacts, some bending is evident, but mostly the films were sheared during the impact, and the result is a higher perforated area.

The susceptibility of the 15 wt.% POSS–PI film to shearing at a temperature of −60 °C is straightforward, and can be explained by the lower degree of chain mobility on one hand, and by the higher stress concentrations that are formed around debonded sites of the POSS aggregates, on the other hand.

The shearing of the 15 wt.% POSS–PI film at 100 °C is somewhat less expected. A plausible explanation is that, at 100 °C, the temperature that is developed during the hypervelocity impact along with the additional applied heat, allow higher chain mobility, which leads to a faster coalescence of the voids that were formed at debonded sites. The coalescence of these voids encourages the shearing of the film under impact at various locations, thus resulting in a large perforated area. The fracture surface, shown in Fig. 2h, can be described as spongy in nature, and the existence of voids is evident. Thus, it can be deduced that debonding of aggregates during the impact of the 15 wt.% POSS–PI sample is the cause for its spongy-like appearance and large perforated area. The same phenomenon also occurs in the case of the 5 wt.% and 10 wt.% POSS–PI samples.

The formation of aggregates during the curing process of the POSS–PI nanocomposite also plays an important role in the reduction of the material's volume electrical resistivity. As shown in Fig. 4, POSS-containing samples demonstrate lower volume electrical resistivity compared to PI. The reduction in electrical resistivity in this case cannot be attributed directly to the amount of POSS added to the PI matrix. The electrical resistivity of a 10 wt.% POSS–PI sample exhibit a small but measurable decrease of about one order of magnitude compared to the electrical resistivity of PI, while the electrical resistivity of 5 wt.% and 15 wt.% POSS–PI is of intermediate values. As shown in Fig. 4, an inverse dependency exists between the POSS aggregates' surface density, ρ_s, and the volume electrical resistivity. A correlation between the aggregates' surface density and the aggregates' bulk density can be assumed from the bulk aggregate distribution shown in Fig. 3. It appears that the distribution of the aggregates in the matrix and their inter-aggregate distance are more prominent factors in the reduction of volume electrical resistivity than the POSS wt.% factor.

The mechanism which leads to the reduction in the volume electrical resistivity can be deduced from the EFM data (Fig. 5). An EFM image (Fig. 5c) reveals the existence of electrical charges (indicated by dark regions) at the interface between the POSS aggregates and the PI matrix. The formation of electrical charges by the electrical field of the EFM tip indicates on regions with lower resistivity at the boundaries of the POSS aggregates. Paths of lower resistivity can also be noticed in radial direction from the POSS aggregates. If the inter-aggregate distance is small enough to allow charge percolation, the volume electrical resistivity will decrease. The 10 wt.% POSS–PI attains the lowest volume electrical resistivity since its aggregates' volume density is the highest and its inter-aggregate distance is the smallest.

5. Conclusions

POSS–PI films were produced with various POSS contents, and their mechanical and electrical properties were evaluated with respect to survival in the LEO environment. The POSS–PI structure includes nanoscale POSS aggregates formed during the curing process. These aggregates are spread on the surface and inside the bulk, affecting both its mechanical and electrical properties.

At RT conditions, hypervelocity impacted POSS–PI is more brittle compared to PI due to debonding of the POSS aggregates from the PI matrix, creating voids which coalescence into critical-size defects. Under extreme temperature conditions, POSS–PI shows higher susceptibility toward hypervelocity impacts, compared to

PI, via formation of a larger perforation area through film shearing. The process of aggregate debonding and voids coalescence apply during extreme temperature conditions as well. Upon impact, coalescence of the voids into critical-size defects occurs, promoting an early failure of the POSS–PI film either at −60 °C or 100 °C. Susceptibility of the POSS–PI film to shearing at a temperature of −60 °C is explained by the lower degree of chain mobility and by the higher stress concentrations, which are established around the aggregates' debonded sites. The shearing effect of the POSS–PI film at 100 °C under hypervelocity impact is related to elevated temperature that allows higher chain mobility, leading to a faster coalescence of the voids that were formed at the debonded sites. The coalescence of the voids encourages the shearing of the film under impact.

The POSS–PI nanostructure also affects its electrical properties. The density of the POSS aggregates and their inter-aggregate distance change the material's volume electrical resistivity. When the inter-aggregate distance is small enough, as in the case of 10 wt.% POSS–PI, the material's volume electrical resistivity decreases to about one order of magnitude the volume electrical resistivity of pure PI. The mechanism which leads to the reduction in volume electrical resistivity is related to the formation of electrically active regions at the interface between the POSS aggregates and the PI matrix, as confirmed by EFM measurements.

References

[1] Bedingfield KL, Leach RD, Alexander MB. NASA reference. Publication 1390; 1996.
[2] Tribble AC. The space environment: implementation for spacecraft design. Princeton, New Jersey: Princeton University Press; 1995.
[3] Grossman E, Gouzman I. Nucl Instrum Methods Phys Res Section B-Beam Interact Mater Atoms 2003;208:48–57.
[4] Silverman EM. Space environmental effects on spacecraft LEO material selection guide. Langley: NASA Langley Research Center; 1995.
[5] Connell JW, Watson KA. High Perform Polym 2001;13:23.
[6] Verker R, Grossman E, Gouzman I, Eliaz N. Polymer 2007;48:19–24.
[7] De Groh KK, Banks BA, McCarthy CE, Rucker RN, Roberts LM, Berger LA. High Perform Polym 2008;20:388–409.
[8] Degroh KK, Banks BA. J Spacecraft Rockets 1994;31:656–64.
[9] Boo WJ, Liu J, Sue HJ. Mater Sci Technol 2006;22:829–34.
[10] Brunsvold AL, Minton TK, Gouzman I, Grossman E, Gonzalez R. High Perform Polym 2004;16:303–18.
[11] Gilman JW, Schlitzer DS, Lichtenhan JD. J Appl Polym Sci 1996;60:591.
[12] Gonzalez RI. Department of chemical engineering, Ph.D.; 2002.
[13] Verker R, Eliaz N, Gouzman I, Eliezer S, Fraenkel M, Maman S, et al. Acta Mater 2004;52:5539–49.
[14] Verker R, Grossman E, Gouzman I, Eliaz N. High Perform Polym 2008;20:475–91.
[15] Ye YS, Chen WY, Wang YZ. J Polym Sci Part a-Polym Chem 2006;44:5391–402.
[16] Seckin T, Koytepe S, Adiguzel HI. Mater Chem Phys 2008;112:1040–6.
[17] Roybal R, Shively J, Stein C, Tolmak P. Cost effective testing for the 21st century. In: Proceedings of the 19th space simulation conference. Baltimore, MD, USA, October 29–31 1996.
[18] Roybal R, Tlomak P, Stein C, Stokes H. Int J Impact Eng 1999;23:811.
[19] Tighe A, Gabriel S, Van Eesbeek M. Materials in space environment. In: Proceedings of the ESA 8th international symposium. Arcachon, France, 5–9 June 2000.
[20] Verker R, Grossman E, Gouzman I, Eliaz N. Compos Sci Technol 2009;69:2178–84.
[21] Du-Pont, Inc. Technical Bulletin, "PYRALIN® Polyimide Coating PI 2545 PI 2540 Product Information"; 1993.
[22] Gheno SM, Kiminami RHGA, Morelli MR, Paulin Filho PI. J Eur Ceram Soc 2010;30:549–54.
[23] Callister WD. Material science engineering. New York: John Wiley & Sons; 2000.
[24] Verker R, Grossman E, Eliaz N. Acta Mater 2009;57:1112–9.
[25] Kim Y, Kang E, Kwon YS, Cho WJ, Cho C, Chang M, et al. Synthetic Met 1997;85:1399–400.
[26] Wang SF, Wang YR, Cheng KC, Chen SH. J Mater Sci: Mater Electron 2010;21:104–10.
[27] Ojeda JR, Martin DC. Macromolecules 1993;26:6557–65.
[28] Li JX, Hiltner A, Baer E. J Appl Polym Sci 1994;52:269–83.
[29] Reynaud E, Jouen T, Gauthier C, Vigier G, Varlet J. Polymer 2001;42:8759–68.
[30] Du-Pont. Inc., T.B. Summary of properties for Kapton® polyimide films; 2008.